Chemistry
A European
Journal

Chemistry Europe
European Chemical Societies Publishing

Accepted Article

Title: High temperature proton conduction in LaSbO4

Authors: Piotr Winiarz, Kacper Dzierzgowski, Aleksandra Mielewczyk–Gryń, Maria Gazda, and Sebastian Wachowski

To be cited as: *Chem. Eur. J.* 10.1002/chem.202004561

Link to VoR: https://doi.org/10.1002/chem.202004561

WILEY-VCH

10.1002/chem.202004561

Graphical abstract

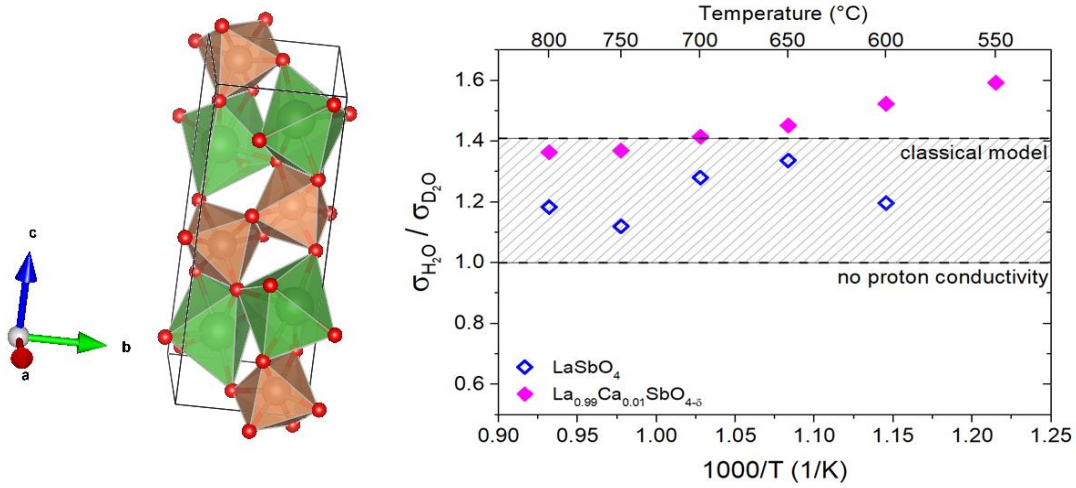

Figure presents the unit cell of synthesized $LaSbO_4$ compound and the result of H/D isotope exchange experiment which proves dominance of protonic conductivity in the material.

10.1002/chem.202004561

High temperature proton conduction in $LaSbO_4$

Piotr Winiarz, Kacper Dzierzgowski, Aleksandra Mielewczyk–Gryń, Maria Gazda and Sebastian Wachowski*

Department of Solid State Physics, Faculty of Applied Physics and Mathematics, Gdańsk University of Technology, Narutowicza 11/12, 80-233 Gdańsk, Poland

*corresponding author: sebastian.wachowski@pg.edu.pl, tel.+48 58 348 66 12, address: Centrum Nanotechnologii A, ul. Narutowicza 11/12, 80-233 Gdańsk

Abstract

Lanthanum ortho-antimonate was synthesized using a solid-state synthesis method. To enhance the possible protonic conductivity, samples with the addition of 1 mol% Ca in La-site, were also prepared. The structure was studied by the means of X-ray diffraction, which showed that both specimens were single phase. The materials crystallized in the space group $P2_1/n$. Dilatometry revealed that material expands non-linearly with the temperature. The nature of this deviation is unknown; however, the calculated linear fraction thermal expansion coefficient was 9.56×10^{-6} 1/K. Electrical properties studies showed that the material is a proton conductor in oxidizing conditions, which was confirmed both by temperature studies in wet in dry air, but also by the H/D isotope exchange experiment. The conductivity was rather modest, peaking at order 10^{-6} S/cm at 800°C, but this can be further improved by microstructure and doping optimization. This is the first time when protonic conductivity in lanthanum ortho-antimonates is reported.

Keywords:

electrical conductivity; fast-ion conductors; proton conducting ceramics; ceramics

Proton Conducting Ceramics (PCCs) are materials exhibiting ionic conductivity in which proton (H^+) is a charge carrier[1]. This class of materials has gathered interest over the years for their potential applications. Especially the so-called triple conducting oxides, i.e. materials with three mobile charge carriers: protons, oxygen ions, and electron/electron holes, were discovered and studied as potential electrode materials[2–5]. The increased interest leads to developing highly-efficient fuel cells [5–7] and steam electrolysers[8]. This interest stems from the fact that PCC-based devices can operate with high efficiencies while being cost-competitive in comparison to traditional Solid Oxide Fuel Cells[5,9]. Apart from that, new types of electrochemical devices have been developed. Such devices can be used for the synthesis of ammonia[10,11], conversion of methane into aromatics in a membrane reactor[12], or thermo-electrochemical production of hydrogen from methane[13].

Typical members of the PCCs are oxides in which upon exposure to humid condition the protonic defect formation occurs according to the hydration reaction (1),

$$H_2O_{(g)} + O_O^x + v_O^{\bullet\bullet} = 2OH_O^{\bullet} \quad (1)$$

In the reaction, two protonic defects $OH_O^{\bullet}$ are formed. Since the acceptor doping promotes the formation of oxygen vacancies $v_O^{\bullet\bullet}$, such doping is introduced in PCCs to increase the concentration of protonic defects and the protonic conductivity. The most known examples of this group of materials belong to the oxides with perovskite structure, namely barium cerate-zirconate solid solutions. Another group of proton-conducting oxides, introduced in 2006 by Haugsrud and Norby[14], is formed by compounds with general formula ABO_4. These ceramics are typically composed of a rare earth metal on the A-site[14–21] and a pentavalent cation from group 5[14–17] or 15[18–22] of the periodic table on the B-site. The highest conductivity, 10^{-3} $S \cdot cm^{-1}$ at 800 °C in wet air, has been achieved for Ca-doped $LaNbO_4$[14] however, this conductivity level is much lower than in the case of the proton-conducting perovskites. Consequently, many attempts have been done to increase the conductivity, mostly by doping/substitution on both A-[23–27] and B-sites[28,29]. Despite all the efforts, it has not been possible yet to increase the conductivity to the desired level. Another problem in the utilization of $LaNbO_4$ is the structural phase transition, occurring at ~500 °C, which is accompanied by the abrupt change of thermal expansion coefficient[30]. This problem can be solved by various doping strategies [17,22,31–33] or by decreasing the grain size[34]. Compounds other than $LaNbO_4$ were also studied, but most of the effort was put on different rare-earth

niobates, tantalates, or phosphates[14,15,21,35]. Our previous works on B-site substituted lanthanum orthoniobate[22,33,36–39] have shown that Sb-substitution decreases the phase transition temperature from 404 ± 5 °C in $LaNb_{0.95}Sb_{0.05}O_4$ to around room temperature in $LaNb_{0.70}Sb_{0.30}O_4$,[22,33] while it does not impede the hydration[39] and proton conductivity either[38].

In this work, we report the structural, microstructural, electrical, and thermal properties of lanthanum orthoantimonate, $LaSbO_4$, and acceptor-doped lanthanum orthoantimonate, $La_{0.99}Ca_{0.01}SbO_{4-\delta}$. For the first time the electrical properties, including the protonic conductivity in this system is reported. Hence, these results are complementary for proton conducting ABO_4 compounds.

$LaSbO_4$ and $La_{0.99}Ca_{0.01}SbO_{4-\delta}$ powders were synthesized via the solid-state reaction route using: La_2O_3 (preheated at 900°C, Alfa, 99.9%), Sb_2O_5 (abcr, 99.9%), and $CaCO_3$ (POCH, 99%) as reagents. Stoichiometric amounts of reagents were mixed in an agate mortar. The milled powders were uniaxially pressed using 350 MPa to obtain 12mm round pellets, which were then sintered at 1400°C for 6h.

Powder X-ray diffraction (XRD) analysis was performed using the Phillips X'Pert Pro MPD with $CuK_{\alpha1}$ and $CuK_{\alpha2}$ radiation. To determine unit cell parameters, XRD patterns were analyzed with the Rietveld refinement method using the HighScore Plus software[40]. As an initial point of the analysis crystal structure of $LaSbO_4$ (space group no. 11, $P2_1/n$)[41] was used.

The dilatometry was performed by Netzsch DIL 402 PC/4 dilatometer in argon in the temperature range 50 – 1000 °C with a heating/cooling rate of 2°C/min. Thermogravimetric (TG) studies were measured on powder samples using Netzsch Tarsus 401 thermobalance in synthetic air in the temperature range 40-900 °C with a heating/cooling rate of 2°C/min.

Micrographs of the cross-section of the pellets were obtained using a FEI Quanta FEG 250 Scanning Electron Microscope (SEM).

The electrical properties were studied by the means of electrochemical impedance spectroscopy (EIS). Gamry Reference 3000 potentiostat was used. The amplitude voltage was set to 1000 mV, and the frequency was swept from 1 Hz to 1 MHz. In the temperature-dependencies measurements, the temperature range of the study was 550–800 °C in dry, H_2O- and D_2O humidified air. The bubblers containing H_2O and D_2O were kept in the room

temperature, 25°C. The water partial pressures of dry, and wet H_2O/D_2O synthetic air, are as follows: $pH_2O_{dry} \approx 6 \cdot 10^{-5}$ atm. for dry air, and $pH_2O_{wet} \approx 0.02$ atm. for H_2O- and D_2O-humidified air. Before the measurements, two circular electrodes were painted using ElectroScience ESL 5542 Pt–paste on each side of the pellets.

The impedance data were deconvoluted in ZView software (Scribner Associates). The equivalent circuit used for deconvolution consists of a resistor R connected in series with multiple (RQ) elements. An (RQ) element is a resistor, R, and a constant phase element, Q, connected in parallel. Each (RQ) element was used as a representation of one of the semicircles (arcs) present in the impedance plots. The impedance Z of the constant phase element is given by the formula:

$$1/Z = Y = Q_0(j\omega)^n \quad (2)$$

where

Y is the admittance, Q_0, and the angle of misalignment, n, are the fitted parameters, j is the imaginary unit, and ω is the angular frequency. Further, the capacitance C related to the process observed in the impedance measurement can be calculated from the formula:

$$C = Q_0^{\frac{1}{n}} R^{\frac{1}{n}-1} \quad (3)$$

The resistance of the crystal grains and grain boundaries was determined using the Brick Layer Model and the capacitances calculated with equation (3), as described in detail by Haile *et al.*[42]. The grain response is typically considered as a process associated to pseudocapacitance values between 10^{-11} and 10^{-12} $F \cdot cm^{-1}$, whereas grain boundaries usually present one or two orders of magnitude higher pseudocapacitances. In this way, the total, grain, and grain boundary conductivities were analysed.

Based on the temperature dependence of the conductivity, the activation energy of the conductivity was calculated by fitting the experimental values to the equation:

$$\sigma T = A exp\left(-\frac{E_A}{kT}\right) \quad (4)$$

where σ refers to a conductivity of any type (total, grain, grain boundary), T - absolute temperature, A - the pre-exponential factor, E_A - activation energy, and k - the Boltzmann constant.

The XRD patterns and the example of Rietveld refinement are presented in Fig.1. All the reflections in the diffraction data of the compounds were indexed with the monoclinic structure (space group $P2_1/n$). The results agree well with the literature reports[41,43,44]. No secondary phases were detected. The Rietveld refinement profile of $LaSbO_4$ is presented in Fig. 1b. The unit cell parameters derived from the refinements as well as other structural data are listed in Tab. 1. Broad peaks are observed in the case of all specimens. It indicates either small crystallite size or relatively high strain in the crystal lattice.

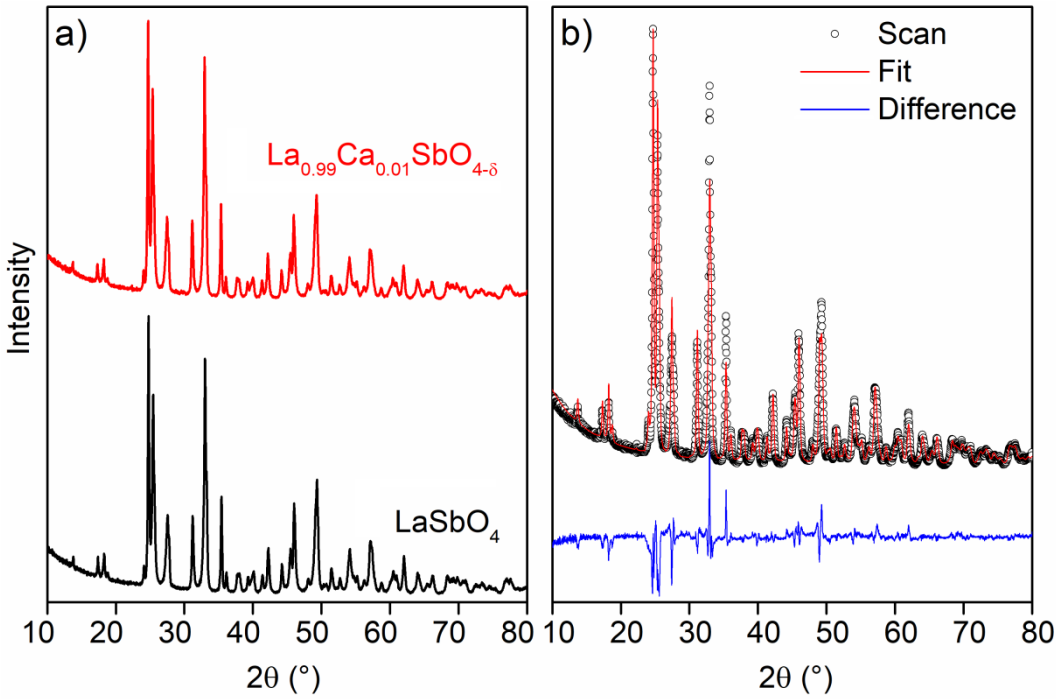

Figure 1 a) X-ray diffractograms of $LaSbO_4$ and $La_{0.99}Ca_{0.01}SbO_{4-\delta}$, and b) Rietveld refinement profile for $La_{0.99}Ca_{0.01}SbO_{4-\delta}$

Table 1. *Structural and microstructural parameters of the synthesized materials. a, b, c, and β, denote the unit cell parameters, V- unit cell volume, R_{wp} – the weighted profile factor of the Rietveld refinement, ρ_{th} – theoretical density, and ρ_{rel} – relative density.*

Compound	a (Å)	b (Å)	c (Å)	β (°)	V (Å^3)	R_{wp} (%)	ρ_{th} (g·cm^{-3})	ρ_{rel} (%)
$LaSbO_4$	5.398	5.067	13.59	109.27	350.99	13.4	6.14	84
$La_{0.99}Ca_{0.01}SbO_{4-\delta}$	5.397	5.066	13.60	109.31	350.86	12.9	6.15	82

The micrographs of the polished fractures of $LaSbO_4$ and Ca-doped sample are shown in Fig. 2. The samples are porous ceramics which is coherent with the results of density measurements (Tab. 1) showing that the density for the antimonates is about 83% of the theoretical density. Both materials have a similar microstructure with average grain size, 2.6 ±

0.5 µm in $LaSbO_4$, and 2.5 ± 0.6 µm in $La_{0.99}Ca_{0.01}SbO_{4-\delta}$. Therefore, the substitution of lanthanum with calcium does not visibly affect the microstructure. In SEM images one can also see pores of the average size around 2 µm.

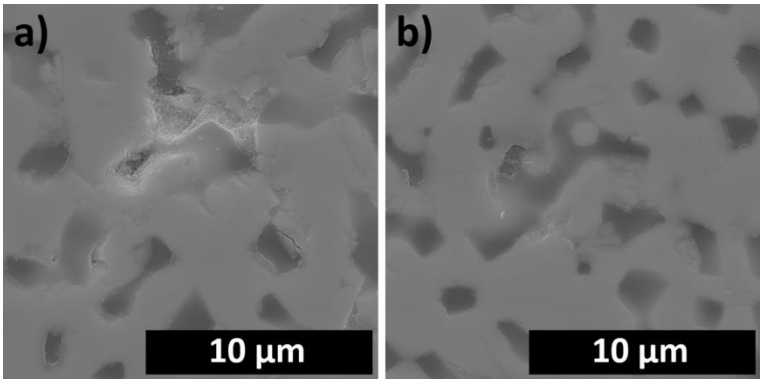

Figure 2. Scanning electron micrographs of polished fractures of a) $LaSbO_4$, and b) $La_{0.99}Ca_{0.01}SbO_{4-\delta}$

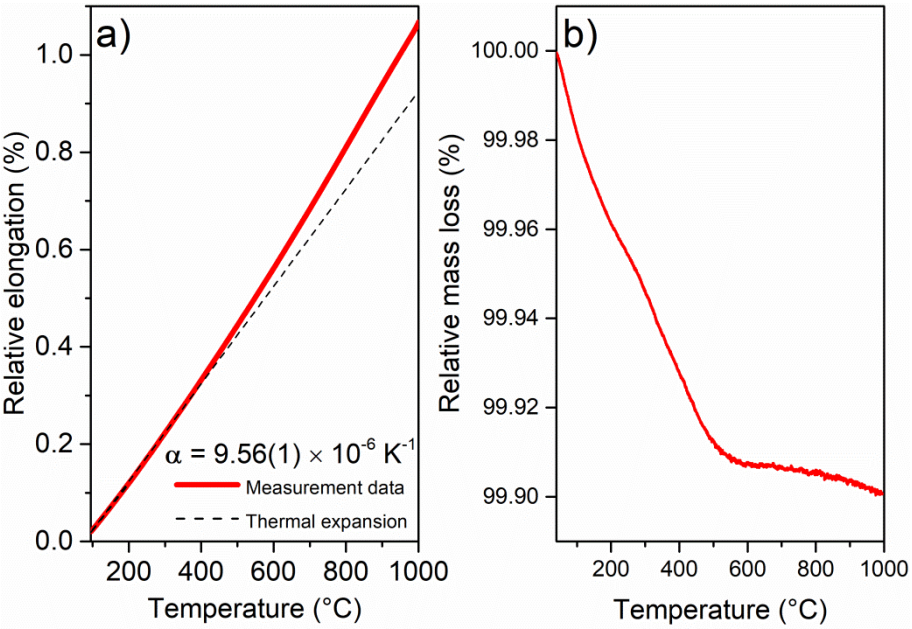

Figure 3. a) Relative elongation vs temperature in argon. Dashed line represents the linear temperature dependence of relative elongation extrapolated into the high-temperature range, b) relative mass loss in synthetic air as a function of temperature for $LaSbO_4$.

The results of the thermal properties measurements are presented in Fig.3. The relative sample elongation as a function of temperature during cooling is shown in Fig. 3a. As can be seen, in the studied temperature range the length of the sample increases, however, at a temperature between 400 and 450 °C a deviation from a linear dependence is observed, which means that the thermal expansion coefficient depends on temperature. Such a temperature dependence

may originate from various temperature-dependent phenomena, for example, changes in ion interactions or structural changes other than bond elongation. It is often described with an experimentally determined polynomial function[45]. Another phenomenon often observed in oxides, contributing to the total linear expansion of the material, is chemical expansion related to the formation of oxygen vacancies at elevated temperatures. Temperatures at which oxygen vacancies may be considered as relevant depend on defect formation energy. In $LaSbO_4$ oxygen vacancy formation requires Sb reduction into Sb^{3+} state. The calculated values for similar system, namely $FeSbO_4$, has been reported to be 3.4 eV[46]. So high energy of defect formation indicates that the contribution of chemical expansion related to oxygen vacancy formation to the total thermal expansion of lanthanum antimonate may be expected at a temperature much higher than 450 °C. It should be noted that the relative mass change above 450 °C (Fig. 3b) is very low. Within the assumption that the thermal expansion coefficient (TEC) is constant in the low-temperature range, TEC determined with the linear fitting of the data below 350 °C equals $9.56(1)\cdot10^{-6}\ {}^{1}/_{K}$. A similar value was obtained ($9.38(1)\cdot10^{-6}\ {}^{1}/_{K}$) because of fitting the temperature dependence of relative elongation with a second-order polynomial.

The relative mass loss of $LaSbO_4$ as a function of temperature during heating in air is presented in Fig. 3b. The sample mass decreases as the temperature increases. In general, the total mass loss (around 0.1 %) of $LaSbO_4$ between room temperature and 1000 °C is low, when compared to other $LaXO_4$ compounds. For example, in $La_{0.98}Mg_{0.02}NbO_{4-\delta}$ relative mass loss observed in the same temperature range was 1.6%[25], whereas in $LaAsO_4$ it was 7%[47]. In the first case, the processes may be attributed to the carbon and carbon dioxide emissions, due to high affinity of lanthanum compounds to CO_2, for the latter it is associated with the dehydration effect, which is more visible at higher temperatures. In lanthanum orthoantimonate, a major part of mass-loss (0.08 %) occurs between room temperature and approximately 550 °C. We suggest that in lanthanum orthoantimonate, the mass losses between approximately 50 and 350 °C, 400, and 700 °C and above 750 °C might be associated with desorption of water, desorption of carbon dioxide and oxygen vacancies formation, respectively. It may be supported by the properties of other $LaXO_4$ compounds. For example, Pradhan and Choudhary[47] studying thermal properties of $LaAsO_4$ with Thermogravimetry (TG) combined with differential scanning calorimetry showed that up to 300 °C mass loss is associated with surface water desorption. Mielewczyk-Gryń et al.[25] in a combined TG and Mass Spectroscopy (MS) experiment found that in Mg-doped $LaNbO_4$

surface water desorption occurs between 100 °C and 360 °C, whereas, between 400, and 700 °C, CO_2 release was observed.

To evaluate electrical properties, EIS measurements as a function of temperature have been performed. An example of a complex impedance plot with a fit, together with an example of pseudocapacitance analysis are presented in Fig. 4. The pseudocapacitance of each (RQ) element was calculated to determine whether the feature observed in the impedance plot represents the conduction processes of the specimen or the electrode responses. The calculated pseudocapacitances of first (RQ) element were in the range of 10^{-11} to 10^{-10} F·cm^{-1} and were independent of the temperature (*cf.* Fig. 4 b). For the second (RQ) element pseudocapacitance includes values in the range of 10^{-8} F·cm^{-1} and the corresponding semicircle was considered as an electrode response and was not taken for further consideration.

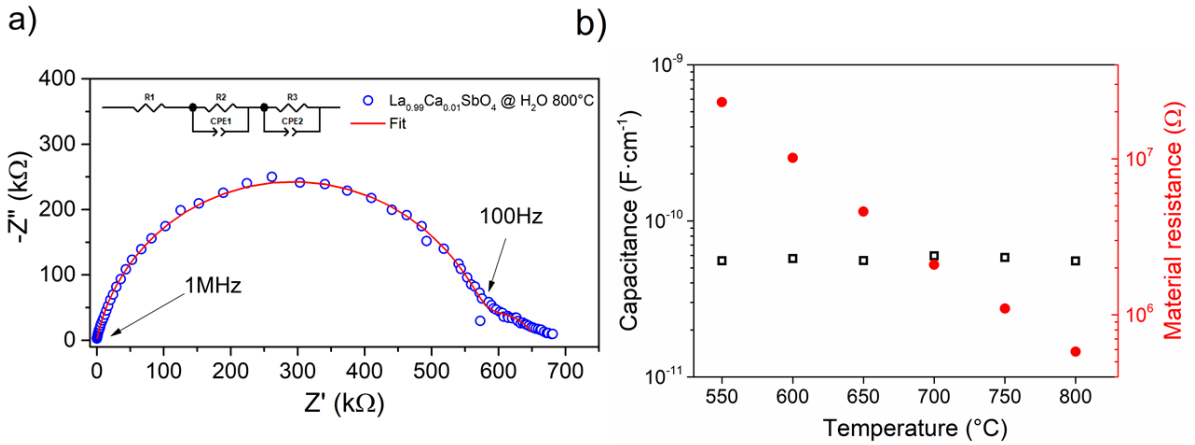

Figure 4. a) Nyquist plot for $La_{0.99}Ca_{0.01}SbO_{4-\delta}$ (open symbols), with the corresponding fit (solid line). The equivalent circuit used for fitting is presented at the top. b) Capacitance vs. temperature for the sample presented in the Nyquist plot corresponding to the material response (left axis), and the material resistance (right axis). Both results correspond to data obtained in the H_2O-humidified atmosphere.

The total conductivity of lanthanum orthoantimonates deconvoluted from EIS data collected in dry, D_2O and H_2O humidified air is presented in Fig. 5a. First, conductivities are between 10^{-7} – 10^{-9} S·cm^{-1} at 550 °C and around 10^{-6} S·cm^{-1} at 800 °C. This is roughly three orders of magnitude lower than in the case of Ca-doped $LaNbO_4$[14]. As expected, the conductivity is thermally activated, however, the apparent activation energy exceeds 1 eV, which is much

10.1002/chem.202004561

higher than 0.5-0.8 eV usually observed for typical proton conduction[14]. This could be a result of the dominance of grain boundaries. In our previous work on Sb-substituted $LaNbO_4$[38] it was shown that while the activation energy of grain conductivity was around 0.5-0.6 eV the respective value for grain boundaries was around 1.3 eV. Since in Sb-substituted niobates total conductivity is dominated by grain boundaries the apparent activation energy of total conductivity was also above 1 eV. Lanthanum orthoantimonates appear to have similar properties. The activation energies of the conductivity of $LaSbO_4$ and $La_{0.99}Ca_{0.01}SbO_{4-\delta}$ are almost the same. This suggests that acceptor doping in this system does not significantly influence the total conductivity, contrary to $LaNbO_4$ where conductivity increased a few orders of magnitudes in Ca-doped samples[27]. Although the reason for it should be confirmed in a separate study on its own some reasons for such a difference could be outlined. One of them could be the low solubility of acceptor dopant which is accompanied by precipitation of a secondary phase in the grain boundaries. This results in a lower-than-expected concentration of the dopant in the bulk. In some cases, this may lead to situation when the effect of doping would not be observed on the conductivity data. Moreover, small amounts of secondary phases (~1 mol %) could not be picked by standard XRD measurement and other techniques, such as synchrotron x-ray diffraction should be used instead. Such effects have been previously observed in ABO_4 materials [48]. Another reason of no apparent effect of doping on conductivity could be defect trapping. For instance, if most of the oxygen vacancies formed by acceptor doping are trapped and are not mobile then they do not contribute to higher conductivity both in dry, due to no new mobile vacancies as a main charge carrier, and wet conditions, due to inability of immobile vacancies to participate in hydration reaction. Then no effect on conductivity would be observed.

10.1002/chem.202004561

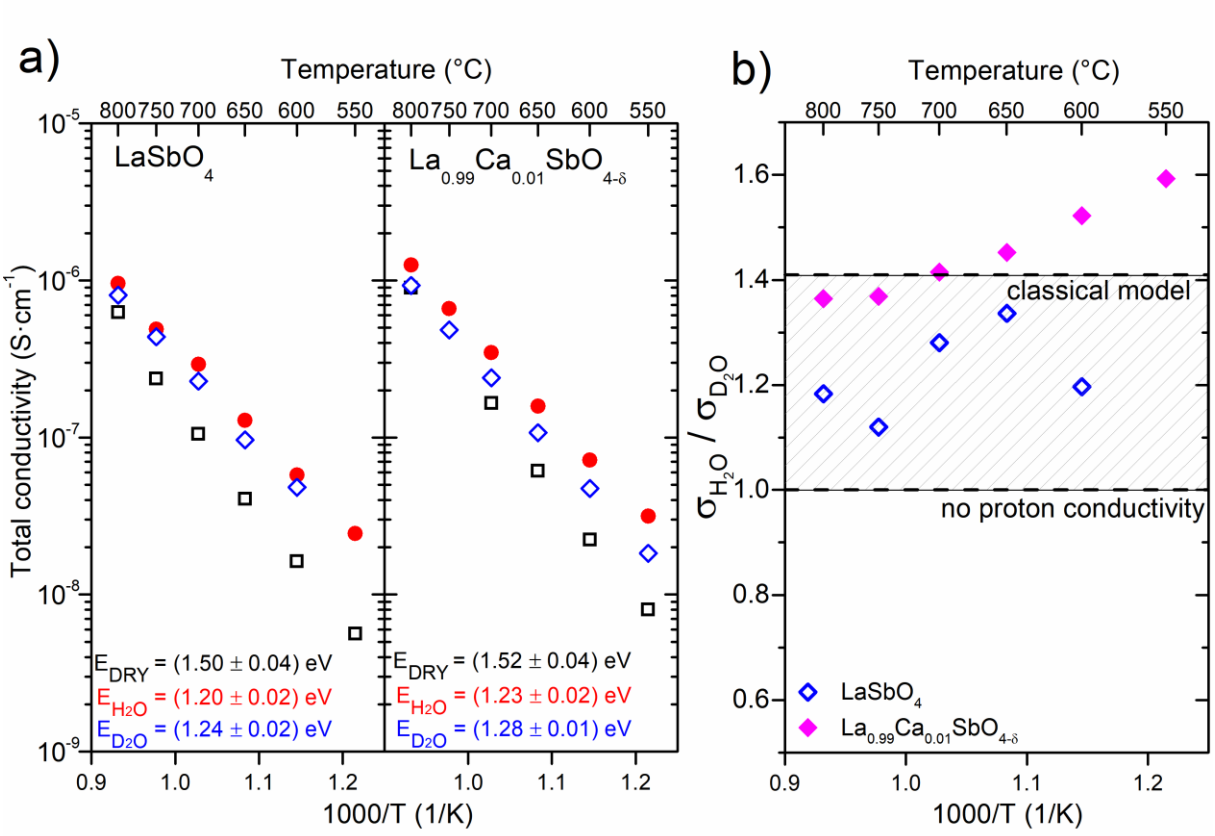

Figure 5. a) Total conductivity presented in the Arrhenius-type plot of $LaSbO_4$ and $La_{0.99}Ca_{0.01}SbO_{4-\delta}$. Red circles – H_2O humidified air, blue diamonds – D_2O humidified air, and black squares – dry air. b) The ratios of total electrical conductivities in H_2O and D_2O-humidified air as a function of temperature for $LaSbO_4$, and $La_{0.99}Ca_{0.01}SbO_{4-\delta}$. Horizontal dashed lines mark the $\sigma H_2O/\sigma D_2O$ equal to $\sqrt{2}$ (classical model of an ideal proton conductor) and 1 (non-proton conductor)

As shown in Figure 5a the conductivity values and activation energies in dry, H_2O- and D_2O-humidified air are different. In both samples, the difference between conductivity in the three atmospheres is noticeable. Below 700°C, the conductivity in H_2O -wet air is at least two times higher than in dry, whereas above this temperature, the difference is lower. This indicates that protons take part in the conduction process in this material. To further examine whether $LaSbO_4$ and $La_{0.99}Ca_{0.01}SbO_{4-\delta}$ are proton conductors, the isotope exchange effect was analysed. In principle, only protonic conductivity is affected by H/D isotope exchange thus if isotope effects are observed in the total conductivity, the material should be dominated by protonic conduction. As can be seen from Fig.5a, the total conductivity in H_2O- is higher than in D_2O- humidified air. In general, two models describe the effects of H/D exchange on conductivity in proton conductors[49]. The classical model limits the consideration of isotope

effect to change of vibration frequency of the O-H(D) bond caused by mass change by exchanging defects from $OH_O^{\bullet}$ to $OD_O^{\bullet}$. In such a case, the conductivity of proton conductor in H_2O-wet atmosphere should be $\sqrt{2}$ times higher than conductivity in D_2O-wet atmosphere. A more accurate quasi-classical model also considers the change of the ground state energy of the proton (deuteron) in the OH(D) group. According to the model, the activation energy of conductivity in the H_2O-wet atmosphere should be roughly 0.05 eV lower[49]. Because in undoped and doped antimonate the activation energy in D_2O- was higher by, respectively, 0.04 eV and 0.05 eV than in H_2O- humidified atmosphere, the quasi-classical model should be applied to these materials. Figure 5b presents $\frac{\sigma_{H2O}}{\sigma_{D2O}}$ ratio, where σ_{H2O} is the total conductivity in H_2O-wet air, and σ_{D2O} is conductivity in D_2O-wet air, plotted as a function of temperature for examined antimonates. In both cases the ratio is higher than unity and decreases with temperature increase. This shows that below 800° C protons have a significant contribution to the total conductivity in $LaSbO_4$ and $La_{0.99}Ca_{0.01}SbO_{4-\delta}$. As may be expected, the $\frac{\sigma_{H2O}}{\sigma_{D2O}}$ ratio is higher in $La_{0.99}Ca_{0.01}SbO_{4-\delta}$ than in the undoped antimonate.

The presence of the isotope effect confirms that in wet conditions protons dominate total conductivity below 800°C. This is similar to the properties of other ABO_4 oxides: such as $LnNbO_4$, $LnTaO_4$[14], $LaAsO_4$[20], or $LaVO_4$[50]. However, the total difference between the conductivity in dry and wet air, smaller than one order of magnitude, indicates a contribution from other charge carriers, i.e., oxygen ions and/or electron holes. These two types of charge carriers are dominant in dry conditions or wet conditions, at temperatures higher than 800 °C. This is consistent with literature findings concerning ABO_4[14,20,38,50].

To sum up; structural, thermal, and electrical properties of $LaSbO_4$ and $La_{0.99}Ca_{0.01}SbO_{4-\delta}$ have been studied. Single-phase undoped and acceptor doped (with 1 mol % Ca) compounds have been obtained. All materials crystallize in monoclinic structure with space group $P2_1/n$. Dilatometry studies have shown that material elongation is a non-linear function of temperature. The calculated linear component of thermal expansion was equal to 9.56×10^{-6} 1/K. The total conductivity of antimonates is dominated by grain boundaries. The effect of acceptor doping was limited, and the conductivity was not increased by a factor higher than 2, however, the Ca addition enhanced protonic conductivity. The H/D isotope exchange experiment confirmed the proton contribution to the total conductivity, and the material shows typical features of the proton conductor. It is the first time that proton conductivity in $LaSbO_4$ is reported.

Acknowledgements

This research work was financially supported by the National Science Centre, Poland Grant No. 2015/17/N/ST5/02813 and 2016/23/B/ST5/02137.

References

[1] M. Marrony, P. Berger, F. Mauvy, J.-C. Grenier, N. Sata, A. Magrasó, R. Haugsrud, P. R. Slater, G. Taillades, J. Roziere, J. Dailly, N. Fukatsu, P. Briois, H. Matsumoto, M. Stoukides, *Proton-Conducting Ceramics. From Fundamentals to Applied Research*, Pan Stanford Publishing, Singapore, **2016**.

[2] T. Miruszewski, K. Dzierzgowski, P. Winiarz, S. Wachowski, A. Mielewczyk-Gryń, M. Gazda, *Materials.* **2020**, *13*, 965.

[3] I. Szpunar, S. Wachowski, T. Miruszewski, K. Dzierzgowski, K. Górnicka, T. Klimczuk, M. H. Sørby, M. Balaguer, J. M. Serra, R. Strandbakke, M. Gazda, A. Mielewczyk-Gryń, *J. Am. Ceram. Soc.* **2020**, *103*, 1809–1818.

[4] R. Zohourian, R. Merkle, G. Raimondi, J. Maier, *Adv. Funct. Mater.* **2018**, *1801241*, 1–10.

[5] C. Duan, J. Tong, M. Shang, S. Nikodemski, M. Sanders, S. Ricote, A. Almansoori, R. OHayre, R. O'Hayre, *Science.* **2015**, *349*, 1321–1326.

[6] S. Choi, C. J. Kucharczyk, Y. Liang, X. Zhang, I. Takeuchi, H.-I. Ji, S. M. Haile, *Nat. Energy* **2018**, *3*, 202–210.

[7] C. Duan, R. J. Kee, H. Zhu, C. Karakaya, Y. Chen, S. Ricote, A. Jarry, E. J. Crumlin, D. Hook, R. Braun, N. P. Sullivan, R. O'Hayre, *Nature* **2018**, *557*, 217–222.

[8] E. Vøllestad, R. Strandbakke, M. Tarach, D. Catalán-Martínez, M.-L. Fontaine, D. Beeaff, D. R. Clark, J. M. Serra, T. Norby, *Nat. Mater.* **2019**, *18*, 752–759.

[9] A. Dubois, S. Ricote, R. J. Braun, *J. Power Sources* **2017**, *369*, 65–77.

[10] S. M. Vasileiou E., Kyriakou V., Garagounis I., Vourros A., *Solid State Ionics* **2015**, *275*, 110–116.

[11] G. Marnellos, M. Stoukides, *Science.* **1998**, *282*, 98 LP – 100.

[12] S. H. Morejudo, R. Zanón, S. Escolástico, I. Yuste-Tirados, H. Malerød-Fjeld, P. K. Vestre, W. G. Coors, A. Martínez, T. Norby, J. M. Serra, C. Kjølseth, *Science.* **2016**,

353, 563–566.

[13] H. Malerød-Fjeld, D. Clark, I. Yuste-Tirados, R. Zanón, D. Catalán-Martinez, D. Beeaff, S. H. Morejudo, P. K. Vestre, T. Norby, R. Haugsrud, J. M. Serra, C. Kjølseth, *Nat. Energy* **2017**, *2*, 923–931.

[14] R. Haugsrud, T. Norby, *Nat. Mater.* **2006**, *5*, 193–196.

[15] R. Haugsrud, T. Norby, *J. Am. Ceram. Soc.* **2007**, *90*, 1116–1121.

[16] R. Haugsrud, T. Norby, *Solid State Ionics* **2006**, *177*, 1129–1135.

[17] Z. Bi, C. A. Bridges, J.-H. Kim, A. Huq, M. P. Paranthaman, *J. Power Sources* **2011**, *196*, 7395–7403.

[18] K. Toyoura, K. Matsunaga, *J. Phys. Chem. C* **2013**, *117*, 18006–18012.

[19] T. Norby, N. Christiansen, *Solid State Ionics* **1995**, *77*, 240–243.

[20] T. S. Bjørheim, T. Norby, R. Haugsrud, *J. Mater. Chem.* **2012**, *22*, 1652–1661.

[21] K. Amezawa, Y. Tomii, N. Yamamoto, *Solid State Ionics* **2003**, *162–163*, 175–180.

[22] S. Wachowski, B. Kamecki, P. Winiarz, K. Dzierzgowski, A. Mielewczyk-Gryń, M. Gazda, *Inorg. Chem. Front.* **2018**, *5*, 2157–2166.

[23] K. Dzierzgowski, S. Wachowski, M. Gazda, A. Mielewczyk-Gryń, *Crystals* **2019**, *9*, 91.

[24] K. Dzierzgowski, S. Wachowski, W. Gojtowska, I. Lewandowska, P. Jasiński, M. Gazda, A. Mielewczyk-Gryń, *Ceram. Int.* **2018**, *44*, 8210–8215.

[25] A. Mielewczyk-Gryn, S. Wachowski, K. Zagórski, P. Jasiński, M. Gazda, *Ceram. Int.* **2015**, *41*, 7847–7852.

[26] H. Fjeld, D. M. Kepaptsoglou, R. Haugsrud, T. Norby, *Solid State Ionics* **2010**, *181*, 104–109.

[27] T. Mokkelbost, I. Kaus, R. Haugsrud, T. Norby, T. Grande, M.-A. Einarsrud, *J. Am. Ceram. Soc.* **2008**, *91*, 879–886.

[28] M. Ivanova, S. Ricote, W. A. Meulenberg, R. Haugsrud, M. Ziegner, *Solid State Ionics* **2012**, *213*, 45–52.

[29] A. D. Brandão, J. Gracio, G. C. Mather, V. V. Kharton, D. P. Fagg, *J. Solid State*

Chem. **2011**, *184*, 863–870.

[30] A. Løken, S. Ricote, S. Wachowski, *Crystals* **2018**, *8*, 365.

[31] F. Vullum, F. Nitsche, S. M. Selbach, T. Grande, *J. Solid State Chem.* **2008**, *181*, 2580–2585.

[32] A. D. Brandão, I. Antunes, J. R. Frade, J. Torre, V. V. Kharton, D. P. Fagg, *Chem. Mater.* **2010**, *22*, 6673–6683.

[33] S. Wachowski, A. Mielewczyk-Gryn, M. Gazda, *J. Solid State Chem.* **2014**, *219*, 201–209.

[34] T. Miruszewski, P. Winiarz, K. Dzierzgowski, K. Wiciak, K. Zagórski, A. Morawski, A. Mielewczyk-Gryń, S. Wachowski, J. Strychalska-Nowak, M. Sawczak, M. Gazda, *J. Solid State Chem.* **2019**, *270*, 601–607.

[35] K. Amezawa, S. Kjelstrup, T. Norby, Y. Ito, *J. Electrochem. Soc.* **1998**, *145*, 3313.

[36] A. Mielewczyk-Gryn, S. Wachowski, J. Strychalska, K. Zagórski, T. Klimczuk, A. Navrotsky, M. Gazda, *Ceram. Int.* **2016**, *42*, 7054–7059.

[37] A. Mielewczyk-Gryn, S. Wachowski, K. I. Lilova, X. Guo, M. Gazda, A. Navrotsky, *Ceram. Int.* **2015**, *41*, 2128–2133.

[38] S. Wachowski, A. Mielewczyk-Gryń, K. Zagórski, C. Li, P. Jasiński, S. J. Skinner, R. Haugsrud, M. Gazda, *J. Mater. Chem. A* **2016**, *4*, 11696–11707.

[39] A. Mielewczyk-Gryń, S. Wachowski, M. Prześniak-Welenc, K. Dzierzgowski, A. Regoutz, D. J. Payne, M. Gazda, D. J. Payne, M. Gazda, *J. Therm. Anal. Calorim.* **2019**, *6*, 225–232.

[40] T. Degen, M. Sadki, E. Bron, U. König, G. Nénert, *Powder Diffr.* **2014**, *29*, S13–S18.

[41] K. P. F. Siqueira, P. Lima, R. A. S. Ferreira, L. D. Carlos, E. M. Bittar, E. Granado, J. C. González, A. Abelenda, R. L. Moreira, A. Dias, *Chem. Mater.* **2014**, *26*, 6351–6360.

[42] S. M. Haile, D. L. West, J. Campbell, *J. Mater. Res.* **1998**, *13*, 1576–1595.

[43] K. P. F. Siqueira, R. L. Moreira, A. Dias, *Chem. Mater.* **2010**, *22*, 2668–2674.

[44] K. P. F. Siqueira, R. M. Borges, J. C. Soares, A. Dias, *Mater. Chem. Phys.* **2013**, *140*, 255–259.

[45] Y. Fei, in *Miner. Phys. Crystallogr. A Handb. Phys. Constants*, **1995**, pp. 29–30.

[46] R. Grau-Crespo, *PhD Thesis* **2006**, 40–82.

[47] A. K. Pradhan, R. N. P. Choudhary, *J. Mater. Sci.* **1987**, *22*, 2955–2958.

[48] G. E. Syvertsen, A. Magrasó, R. Haugsrud, M. A. Einarsrud, T. Grande, in *Int. J. Hydrogen Energy*, **2012**, pp. 8017–8026.

[49] N. Bonanos, A. Huijser, F. W. Poulsen, *Solid State Ionics* **2015**, *275*, 9–13.

[50] M. Huse, T. Norby, R. Haugsrud, *J. Electrochem. Soc.* **2011**, *158*, B857–B865.